Absolute photoionization cross sections for Xe^{4+}, Xe^{5+}, and Xe^{6+} near 13.5 nm: Experiment and theory

A. Aguilar* and J. D. Gillaspy†
National Institute of Standards and Technology, Gaithersburg, Maryland 20899–8421, USA

G. F. Gribakin‡
Department of Applied Mathematics and Theoretical Physics, Queen's University, Belfast BT7 1NN, Northern Ireland, United Kingdom

R. A. Phaneuf§ and M. F. Gharaibeh
Department of Physics, MS 220, University of Nevada, Reno, Nevada 89557-0058, USA

M. G. Kozlov
Petersburg Nuclear Physics Institute, Gatchina 188300, Russia

J. D. Bozek‖ and A. L. D. Kilcoyne
Advanced Light Source, Lawrence Berkeley National Laboratory, Berkeley, California 94720, USA
(Received 21 December 2005; published 20 March 2006)

Absolute photoionization cross-section measurements for a mixture of ground and metastable states of Xe^{4+}, Xe^{5+}, and Xe^{6+} are reported in the photon energy range of $4d \rightarrow nf$ transitions, which occur within or adjacent to the 13.5 nm window for extreme ultraviolet lithography light source development. The reported values allow the quantification of opacity effects in xenon plasmas due to these $4d \rightarrow nf$ autoionizing states. The oscillator strengths for the $4d \rightarrow 4f$ and $4d \rightarrow 5f$ transitions in Xe^{q+} ($q=1-6$) ions are calculated using nonrelativistic Hartree-Fock and random phase approximations. These are compared with published experimental values for Xe^{+} to Xe^{3+} and with the values obtained from the present experimental cross-section measurements for Xe^{4+} to Xe^{6+}. The calculations assisted in the determination of the metastable content in the ion beams for Xe^{5+} and Xe^{6+}. The experiments were performed by merging a synchrotron photon beam generated by an undulator beamline of the Advanced Light Source with an ion beam produced by an electron cyclotron resonance ion source.

DOI: 10.1103/PhysRevA.73.032717 PACS number(s): 32.80.Fb, 32.80.Dz, 32.70.Cs

I. INTRODUCTION

The development of extreme ultraviolet (EUV) light sources for the next generation of lithography technology is presently facing many challenges, one of which is the feasibility of generating more than 100 W of power in a narrow (2%) wavelength band centered at 13.5 nm [1]. Xenon liquid and gas targets are being extensively explored experimentally as the active emitter in prototypes of EUV lithography (EUVL) light sources based on discharge-produced plasmas (DPP) [2,3] and laser-produced plasmas (LPP) [4,5]. Comparisons between these types of sources may be found elsewhere [6,7]. Complex computational codes are being developed [8–10] to model such types of sources. These codes face the challenge of including all relevant atomic processes. The photoionization of singly and multiply charged ions is an important atomic process in many plasmas, including DPP and LPP. For instance, it is thought that in DPP, the photoionization of low-charged ions and neutrals plays an essential role in the so-called bypass currents [11], and thus absolute photoionization cross-section values are needed to determine the magnitude of this effect. In the case of many LPP sources, it is known that the EUV light originates from a thin shell at the surface of the plasma [12,13], and absolute photoionization cross-section values for the ionic species surrounding the plasma are required for the determination of the plasma opacity. Moreover, accurate photoionization cross sections are excellent benchmarks to test the overall implementation of the atomic physics in the complex codes that are being devoted to support EUV light source development [14].

Absolute photoionization cross sections for some of the low-charged xenon ions have been reported previously by different groups. Xe^{+} was studied independently by Andersen *et al.* [15] and by Itoh *et al.* [16]. Within the experimental errors, the two sets of cross sections agree over the energy range from 70 to 130 eV. In both cases, the aim of the study was to investigate quantitative changes of the 4*d* photoionization process along the first member of the xenon iso-

*Present address: Jet Propulsion Laboratory, California Institute of Technology, Pasadena, CA 91109, USA; E-mail address: alex.aguilar@jpl.nasa.gov
†E-mail address: john.gillaspy@nist.gov
‡E-mail address: g.gribakin@am.qub.ac.uk
§E-mail address: phaneuf@physics.unr.edu
‖Present address: Stanford Linear Accelerator Center, Menlo Park, CA 94025

nuclear sequence. They found that the absolute photoionization cross sections for Xe and Xe^+ in the energy region of the giant resonance are nearly the same, concluding that the removal of only one outer electron has little effect on the magnitude of the total photoionization cross section within the $4d$ threshold energy region. Andersen *et al.* [15] also reported the absolute photoionization cross sections for Xe^{2+}, drawing the same conclusion. Photoion yields for Xe^{3+} were reported by Koizumi *et al.* [17] and recently, with much higher resolution, absolute photoionization cross sections were measured by Emmons *et al.* [18,19]. Bizau *et al.* [20] reported photoion yields for Xe^{4+} to Xe^{7+} accompanied by multiconfiguration Dirac-Fock (MCDF) calculations. However, no absolute photoionization cross sections for these ions have been reported.

All the previous experiments have in common the use of the merged-beams technique pioneered in 1973 by Peart *et al.* [21] for measuring electron-impact cross sections and applied in 1986 to photoionization cross-section measurements for singly charged ions by Lyon *et al.* [22]. The continual improvements in synchrotron radiation light sources as well as ion sources have made it possible in recent years to improve the accuracy of these types of measurements and to extend studies to highly charged ions. At the present time, a number of synchrotron radiation facilities around the world [20,23–25] have merged-beams apparatus dedicated to measuring absolute photoionization cross sections for positive and negative ions. For a recent review of the experimental work performed during the last decade, the reader is referred to a paper by West [26].

Photoabsorption by the $4d^{10}$ subshell is dominated by the strong $4d \rightarrow nf$, εf transition. It possesses a number of interesting features defined largely by the nature of the final state. (The $4d \rightarrow np$, εp transition is relatively weak.) For neutral atoms between Pd and Cs the $4d \rightarrow nf$, εf strength lies almost entirely in the continuum, forming a broad maximum of ~25 Mb about 30 eV above the $4d$ ionization threshold. This feature is caused by a specific double-well shape of the effective potential for the f electrons due to an interplay between the repulsive centrifugal and attractive screened nuclear potentials. The inner well of the potential for these atoms is not deep enough to support a bound state. However, it possesses an f-wave resonance. The resonance wave function has a strong overlap with the $4d$ subshell, which results in the "giant" resonant maximum in the $4d$ photoabsorption.

Moving from Cs to Ba, La and lanthanides, one observes a rapid and dramatic change in the $4d$ photoabsorption. The $4d$ oscillator strength is shifted from the continuum to the discrete nf states, in particular, $4f$. This change is driven by the deepening of the potential for the f-wave electron. It follows a transformation of a diffuse Rydberg-type $4f$ orbital into a tightly bound valence-type wave function with a strong overlap with the $4d$ subshell. This transformation occurs rapidly and is known as the "collapse" of the $4f$ orbital. Simultaneously, strong discrete lines become the dominant feature of the $4d$ photoabsorption. A similar effect takes place if an atom with $Z \leqslant 56$ (e.g., Ba, Cs, Xe or, say, Sn) is ionized. It has been studied widely for a number of ions (see, e.g., Ref. [27,28] and references therein), including Xe^+ and Xe^{2+} [15].

In this paper, an important step further is taken in the investigation of the $4d \rightarrow nf$ transitions by measuring absolute photoionization cross sections for Xe^{4+}, Xe^{5+}, and Xe^{6+} in the energy ranges where $4d \rightarrow nf$ transitions occur. The oscillator strengths for the $4d \rightarrow 4f$ and $4d \rightarrow 5f$ transitions in Xe^{q+} $(q=1-6)$ ions are calculated using nonrelativistic Hartree-Fock (HF) and random phase approximations (RPA) and compared with the values obtained from measurements. All the experiments were performed using the ion-photon beam (IPB) endstation permanently installed at beamline 10.0.1 of the Advanced Light Source at the Lawrence Berkeley National Laboratory [25].

II. EXPERIMENT

A detailed description of the IPB endstation may be found elsewhere [25], and only a brief account is presented here. The xenon ions are produced in an electron cyclotron resonance (ECR) ion source and accelerated by a potential of (6.0 ± 0.1) kV. The ion beam is directed to a 60° analyzing magnet where the desired ion charge state is selected. This primary ion beam is merged by a 90° spherical electrostatic deflector onto the axis of a counter-propagating beam of monochromatized synchrotron radiation. A cylindrical einzel lens focuses the beam in the center of the interaction region, which consists of an isolated stainless-steel-mesh cylinder biased at typically $(+2.0 \pm 0.1)$ kV. This potential energy tags the photoions produced in the interaction region by accelerating the product ions and leaving the primary ion beam energy unchanged. Closely spaced pairs of grounded apertures at the entrance and exit of the biased cylinder accurately define a length of (29.4 ± 0.3) cm as the effective interaction region. Subsequently, an analyzing magnet demerges the beams and directs the photoions produced inside the biased cylinder to a single-particle detector, while the primary ion beam is directed into a Faraday cup.

Two different modes of operation of the IPB endstation were used for the collection of the data reported. First, the photoion-yield spectra as a function of photon energy were obtained by setting the interaction region bias voltage to zero, maximizing the merged path. Second, absolute cross-section measurements were performed at a number of discrete photon energies. For the absolute measurements, the interaction region was biased at +2.0 kV, accurately defining the interaction length and energy-labeling the photoions produced inside this region. At each discrete photon energy $(h\nu)$, the value of the total absolute photoionization cross section σ_{pi} in cm^2 is determined from experimentally measured parameters:

$$\sigma_{pi}(h\nu) = \frac{Rqe^2 v_i \epsilon}{I^+ I^\gamma \Omega \delta \Delta \int F(z) dz}, \tag{1}$$

where R is the photoion count rate $[s^{-1}]$, q is the charge state of the parent ion, $e = 1.6 \times 10^{-19}$ C, v_i is the ion beam velocity inside the interaction region [cm/s], ϵ is the responsivity of the photodiode [electrons/photon], I^+ is the primary ion

TABLE I. Typical experimental parameters with their estimated random and systematic uncertainties for absolute photoionization cross-section measurements for Xe^{6+} at a photon energy of 98.4 eV.

Parameter	Value(s)	Uncertainties random	systematic	Total
Ion beam current, I^+	11.4 nA		2%	2%
Photodiode current, I^γ	79.3 μA	2%	2%	3%
Ion interaction velocity, v_i	2.3×10^7 cm/s		5%	5%
Xe^{7+} signal rate, R	1902 s^{-1}	3%		3%
Form factors: $F(z_1),F(z_2),F(z_3)$	14.1, 7.12, 5.16 cm^{-2}	10%	7%	12%
Beam overlap integral, $\int F(z)dz$	264 cm^{-1}	16%	7%	17%
Photodiode responsivity, ϵ	24.4 electrons/photon	3%	6%	7%
Merge-path length, L	29.4 cm		3%	3%
Pulse transmission fraction, δ	0.91		3%	3%
Photoion collection efficiency, Ω	1	2%	2%	3%
Photoion detection efficiency, Δ	1		5%	5%
Cross section, σ	887×10^{-18} cm^2	19%	15%	24%

beam current [A], I^γ is the photodiode current [A], Ω is the photoion collection efficiency, δ is the pulse transmission fraction of the photoion detection electronics (determined by the pulse-discriminator setting), Δ is the measured absolute photoion detection efficiency, and the beam overlap integral $\int F(z)dz$ defines the spatial overlap of the photon and ion beams along the common interaction path in units of cm^{-1}. The propagation direction of the ion beam is defined as the z axis. At each of the three positions z_i at which beam intensity profiles were measured, the form factor $F(z_i)$ was determined by the following relation:

$$F(z_i) = \frac{\int\int I^+(x,y)I^\gamma(x,y)dx\,dy}{\int\int I^+(x,y)dx\,dy \int\int I^\gamma(x,y)dx\,dy}. \qquad (2)$$

The profiles were measured at each of the three positions z_i and form factors $F(z_i)$ were calculated using Eq. (2). The beam overlap integral in Eq. (1) was then determined by interpolation of the $F(z_i)$ to obtain $F(z)$ and integrating along the length of the biased interaction region. Table I shows typical experimental parameters used for absolute cross-section measurements for Xe^{6+}. Estimated systematic and random uncertainties for the parameters in Eq. (1) are also indicated in this table at 95% confidence level. The total uncertainty for an absolute cross-section measurement is the quadrature sum of these uncertainties. At each discrete photon energy, several measurements were obtained in order to reduce the total random uncertainty.

Typical photon fluxes of 2.0×10^{13} photons/sec were used for this experiment. The accuracy of the photon energy scale for all measurements is estimated to be 100 meV. The energy scale was calibrated by measuring the $4d\rightarrow4f$ resonant transition in Xe^{3+} and referencing to measurements made by Emmons *et al.* [18], for which the calibration was based on careful gas-cell measurements of well-known resonances in gases [29,30].

Absolute measurements rely heavily on accurate photon and ion detector calibrations. A batch-calibrated Si photodiode traceable to NIST with a quoted uncertainty of 5% was used as a photon detector. Two identical photodiodes were installed and gave consistent measurements within ±2%. The detection efficiency is obtained by measuring the product ion current using an averaging subfemtoammeter, and comparing it to the measured count rate. This extremely sensitive measurement required operating the detector alternately as a Faraday cup and as a single-particle detector. The absolute detection efficiency of the photoion detector was not determined for the ionic species under study but it has periodically been measured for a variety of ions ranging from singly charged ions to multiply charged ions. A consistent value of 0.95 ± 0.05 has been obtained for all ions of similar velocity and charge +2 and above. This efficiency value is considerably higher than that reported in Covington *et al.* [25] due to the use of a double microchannel plate in the present work as opposed to a microsphere plate used previously.

III. THEORY

The total integral oscillator strength of the $4d\rightarrow nf,\varepsilon f$ transition is close to 10 (the number of $4d$ electrons). It accounts for most of the strength of the $4d$ photoabsorption. In order to describe $4d$ photoabsorption theoretically, one needs to use an accurate potential for the f electron. In particular, the strong exchange interaction must be included correctly, e.g., by coupling the dipole-excited f electron and $4d$ hole into the ^1P term (in LS scheme) in the Hartree-Fock approximation. Another important effect which is *beyond* any single-particle (e.g., Hartree-Fock) approximation is a collective response of the ten $4d$ electrons to the photon field. This *electron correlation* effect means that an electron can be removed from a many-electron target not only after directly absorbing a photon, but also after a change in the mean field of the atom in the electromagnetic wave. Such a correlation

TABLE II. Oscillator strengths of $4d \rightarrow 4f$ and $4d \rightarrow 5f$ transitions in Xe^{q+} ions. Best predictions are shown in boldface.

		I_{4d}	ω_{4d-4f}	f_{4d-4f}		ω_{4d-5f}	f_{4d-5f}	
Ion	Calc. type	(eV)	(eV)	*L*	*V*	(eV)	*L*	*V*
Xe^{6+}	HF	149.8	102.3	7.39	4.46	118.7	2.88	1.59
	RPA, 1 ch.[a]		100.8	6.70	6.37	117.8	1.94	1.86
	RPA, 5 ch.[b]		100.7	**6.78**	6.55	117.8	**1.97**	1.88
Xe^{5+}	HF	135.3	99.6	5.95	3.61	112.4	2.66	1.52
	RPA, 1 ch.[a]		98.5	5.62	5.22	111.7	2.00	1.87
	RPA, 4 ch.[c]		98.2	**5.43**	5.06	111.6	**1.96**	1.84
Xe^{4+}	HF	121.6	96.4	4.28	2.60	105.7	2.10	1.24
	RPA, 1 ch.[a]		95.7	**4.24**	3.88	105.2	**1.76**	1.63
Xe^{3+}	HF	108.7	92.7	2.45	1.50	98.6	1.36	0.82
	RPA, 1 ch.[a]		92.3	**2.60**	2.35	98.3	**1.30**	1.19
Xe^{2+}	HF	96.7	88.1	0.78	0.49	91.1	0.58	0.35
	RPA, 1 ch.[a]		88.0	**0.89**	0.80	91.1	**0.63**	0.57
Xe^{+}	HF	85.6	82.0	0.058	0.035	83.3	0.055	0.033
	RPA, 1 ch.[a]		82.0	**0.062**	0.054	83.3	**0.059**	0.052

[a]Calculation includes one channel: $4d \rightarrow nf, \varepsilon f$.
[b]Calculation includes five channels: $5s \rightarrow np, \varepsilon p$; $4d \rightarrow nf, \varepsilon f$; $4d \rightarrow np, \varepsilon p$; $4p \rightarrow nd, \varepsilon d$; and $4p \rightarrow ns, \varepsilon s$.
[c]Calculation includes four channels: $4d \rightarrow nf, \varepsilon f$; $4d \rightarrow np, \varepsilon p$; $4p \rightarrow nd, \varepsilon d$; and $4p \rightarrow ns, \varepsilon s$.

is accounted for by the random phase approximation (RPA). This method and its modifications have been powerful tools for understanding many features of atomic photoabsorption (see, e.g., Refs. [31,32]). In particular, it was used recently to study the photoionization cross sections of Xe^{+} and Xe^{2+} [15,33], and applied earlier to the photoionization of neutral Xe and Ba above the $4d$ threshold ([34], and references therein).

Table II shows the oscillator strengths of $4d \rightarrow 4f$ and $4d \rightarrow 5f$ lines calculated using nonrelativistic HF and random phase approximations for Xe^{6+} through to Xe^{+}. Strictly speaking, RPA can only be applied to systems with closed subshells, or those with a single electron above closed shells (although, some generalizations to open-shell systems have been developed [32]). In the present calculations for ions with one or more electrons in the $5p$ subshell, the $5p$ electrons have been treated as spectators. Their average field contributes to the potential acting on the f electron and affects the excitation energy, while the important $4d^9nf\ ^1P$ coupling is preserved. The main photoabsorption strength of the $5p$ and $5s$ subshells lies at much lower energies than those of the $4d \rightarrow nf$ lines. Hence, these electrons have only a small dynamical effect on the strength of the $4d \rightarrow nf$, εf transitions. This is why one can expect to obtain reliable estimates of the $4d \rightarrow nf$ oscillator strengths from single-channel RPA calculations.

The difference between the results obtained with the length (L) and velocity (V) forms of the dipole operator in the HF approximation shows the size of electron correlation effects. Theoretically, in full RPA the two forms should give identical answers (for a closed-shell system). The discrepancy between RPA L and V results in Table II reflects the uncertainty of the numerical calculation (e.g., due to a finite number of Rydberg states or a limited number of channels). To test the role of relativistic effects, relativistic configuration-interaction (CI) calculations of these transitions in Xe^{6+} and Xe^{5+} were also performed as explained in the next section.

IV. RESULTS

A. Photoionization of Xe^{6+}

The RPA method is fully applicable to (and, hence, more reliable for) systems with closed shells, such as Xe^{6+} $4d^{10}5s^2$, and we examine this ion first. As seen from Table II, the best HF calculation of the $4d^95s^2nf\ ^1P$ excited states, gives L and V oscillator strengths that differ by almost a factor of 2. In contrast, the RPA calculation which includes a single channel, $4d \rightarrow nf$, εf, brings the L and V results within about 10% of each other. Note that the correlation contribution is especially large for the oscillator strength in the V form. RPA corrections also produce a sizeable shift in the transition energies $\omega_{4d \rightarrow 4f}$ and $\omega_{4d \rightarrow 5f}$. The $4d \rightarrow nf$, εf channel is by far the strongest photoabsorption channel in this photon energy range. Other channels have relatively little influence on the $4d \rightarrow nf$ oscillator strengths (especially in the L form). Thus, the largest five-channel calculation gives values of $f^{(L)}_{4d \rightarrow 4f}$ and $f^{(L)}_{4d \rightarrow 5f}$ within 1% to 2% of the one-channel results.

Since the $4d \rightarrow nf$ transition energies lie above the ionization threshold of the Xe^{6+} ion, the $4d^95s^2nf$ states autoionize into the $4d^{10}5s\varepsilon p$ channel. Figure 1 shows the measured and calculated photoionization cross section for Xe^{6+} with promi-

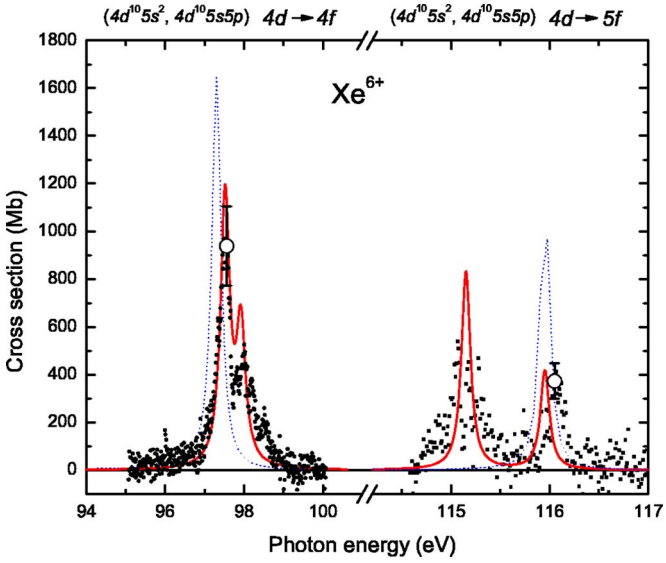

FIG. 1. (Color online) Absolute photoionization cross section for Xe^{6+} ions. The open circles indicate our measured absolute photoionization cross section to which the experimental photoion-yield (small dots) spectrum measured at an energy resolution of 60 meV is normalized. The dotted (blue) curve corresponds to the $5s$ photoionization cross section of Xe^{6+} from the five-channel RPA calculation (L form) including $5s \rightarrow np, \varepsilon p$, $4d \rightarrow nf, \varepsilon f$, $4d \rightarrow np, \varepsilon p$, $4p \rightarrow nd, \varepsilon d$, and $4p \rightarrow ns, \varepsilon s$. The solid (red) curve contains the RPA oscillator strength of these transitions and RPA autoionizing widths where the contributions of the ground and metastable species have been weighted by $\frac{2}{3}$ and $\frac{1}{3}$, respectively (see Table III).

nent $4d \rightarrow nf$ resonances. The open circles with error bars denote our absolute measurements to which the experimental photoion-yield spectrum is normalized. The calculated cross sections of the $4d \rightarrow 4f$ and $4d \rightarrow 5f$ resonances are shown by dotted curves. Their autoionizing widths are 0.277 and 0.110 eV, respectively. These values were obtained together with the corresponding transition energies and oscillator strengths in Table II by fitting the resonances with Breit-Wigner profiles.

Figure 1 shows that the simple Breit-Wigner shapes of the $4d \rightarrow 4f$ and $4d \rightarrow 5f$ lines predicted by RPA are quite different from the experimental data. Indeed, the experimental data of Fig. 1 suggest that the $4d \rightarrow 4f$ transition contains contributions of two lines, a stronger one at 97.5 eV, and a weaker one at 98 eV. Likewise, in the same figure, the $4d \rightarrow 5f$ clearly shows two lines at 115.3 and 116.1 eV, the former, with its own internal structure. In principle, such additional structure in the lines could be caused by the spin-orbit splitting of the $4d$ orbital (whose magnitude is equal to 2 eV [35]). To explore this question theoretically, relativistic Dirac-Fock (DF) and CI calculations of the relevant transitions were performed [36,37]. The DF ionization potentials of the two fine-structure components of the $4d$ subshell are $I_{4d_{5/2}} = 146.6$ eV and $I_{4d_{3/2}} = 148.7$ eV. This splitting, however, is much smaller than the $4d \rightarrow 4f$ and $4d \rightarrow 5f$ exchange interaction. As a result, both dipole transitions give rise to a single dominant line ($^1P_1$ term), as one would expect in the LS-coupling scheme. The transition energies and oscillator strengths obtained from the relativistic CI calculations are reported in Table III.

TABLE III. Transition energies and oscillator strengths of the $4d \rightarrow 4f$ and $4d \rightarrow 5f$ transitions in Xe^{6+} from the relativistic CI calculations.

Initial state	ω_{4d-4f}	f_{4d-4f}		ω_{4d-5f}	f_{4d-5f}	
	(eV)	L	V	(eV)	L	V
$Xe^{6+}4d^{10}5s^2\ ^1S_0$	100.9	6.9	4.5	117.0	2.8	1.7
$Xe^{6+}4d^{10}5s5p\ ^3P_0$	101.3	6.9	4.5	117.8[a]	2.3	1.4

[a]The $4d \rightarrow 5f$ transition in the metastable ion, $Xe^{6+}5s5p^3P_0$, gives rise to a few satellites, the strongest of which, at 117.0 eV, has the oscillator strengths of 0.19 (L) and 0.11 (V).

The CI calculations contained a relatively small number of excited-state configurations $4d^9 5s^2 nf$ ($n=4,5,6,7$) with physical $4f$ and $5f$ DF orbitals, and pseudo-orbitals for $n=6,7$ (to take some account of higher n and εf continuum). Important RPA-type correlations remain beyond this CI scheme, which resulted in a marked difference between the L and V oscillator strengths [38]. This difference and the values of $f_{4d \rightarrow 4f}$, as well as the transition energies, are similar to those obtained in the nonrelativistic HF approximation (Table II). Most importantly, the relativistic calculation confirms that the $4d \rightarrow 4f$ and $4d \rightarrow 5f$ transitions have a simple single-line shape. Thus, relativistic effects cannot explain the two-peak structures observed experimentally in each of the transitions.

It is, however, possible that the ion beam contained a fraction of ions in metastable states, e.g., $Xe^{6+}\ 5s5p\ ^3P_0$. The $4d \rightarrow nf$ lines in the metastable ions can be shifted with respect to their ground-state positions. In principle, the lines can also have a more complicated structure. To investigate this possibility, the $4d \rightarrow nf$ excitation energies and oscillator strengths from the lowest metastable state, $Xe^{6+}\ 5s5p\ ^3P_0$, were calculated (see Table III). In spite of a larger number of possible final states (due to the open-shell nature of the initial state) we observe that both the $4d \rightarrow 4f$ and $4d \rightarrow 5f$ transitions due to the ($^3P_0$) metastable contain essentially a single strong peak. Their oscillator strengths have changed little, although the main $4d \rightarrow 5f$ line has lost part of its oscillator strength to a few weaker lines. What is important though, is that the energies of the main $4d \rightarrow 4f$ and $4d \rightarrow 5f$ lines in $Xe^{6+}\ 5s5p\ ^3P_0$ are upshifted by 0.4 and 0.8 eV, respectively, relative to the lines in the ground-state Xe^{6+}. These shifts are comparable to the spacings between the principal and secondary peaks in Fig. 1. Therefore, the structure of the $4d \rightarrow 4f$ and $4d \rightarrow 5f$ transitions observed in the experiment can be considered as evidence that the Xe^{6+} beam contained about 30% of long-lived metastable states ($5s5p\ ^3P_0$). The solid line in Fig. 1 corresponds to the $4d \rightarrow 4f$ and $4d \rightarrow 5f$ resonances in $Xe^{6+}\ 5s^2$ and $Xe^{6+}\ 5s5p\ ^3P_0$, with the RPA oscillator strength of these transitions and RPA autoionizing widths. The contributions of the ground and metastable species have been weighted with $\frac{2}{3}$ and $\frac{1}{3}$, respectively. Note that the energies of the $4d \rightarrow 4f$ and $4d \rightarrow 5f$ transitions from either RPA (Table II) or CI

calculation (Table III) are a few eV higher than those observed in experiment. Their downshifts due to correlations (RPA vs HF) or relativistic effects (present CI vs HF) are about 1.5 eV. However, neither calculation accounts fully for both effects and therefore downshifts of these magnitudes are to be expected. Hence, for the purpose of comparison with experiment, the theoretical curves in Fig. 1 have been shifted by −3.38 and −1.85 eV for the $4d \rightarrow 4f$ and $4d \rightarrow 5f$ lines, respectively.

B. Photoionization of Xe^{5+}

RPA can also be applied in a rigorous way to systems with one electron above the closed shells like $Xe^{5+}4d^{10}5s^25p$. However, given the small effect of all channels other than $4d \rightarrow nf$, εf on the $4d \rightarrow nf$ strengths, we estimate these strengths for Xe^{q+} $(q=1-5)$ from single-channel RPA calculations. The exception is made for Xe^{5+} where a four-channel result is also shown in Table II.

The shapes of the measured cross sections in the $4d \rightarrow 4f$ (Fig. 2) and $4d \rightarrow 6f$ (not shown) regions in Xe^{5+} also indicate that they consists of a number of individual lines. To analyze this structure, relativistic CI calculation of the excited states of Xe^{5+} were performed. They included 32 configurations of the type $4d^95s^25pnf$, with physical orbitals for $n=4,5$ and pseudo-orbitals for $n=6,7$. The ground state of Xe^{5+} is $4d^{10}5s^25p\ ^2P_{1/2}$. There is also a metastable state $4d^{10}5s^25p\ ^2P_{3/2}$, lying 1.95 eV above it. The $5^2P_{3/2}$ state decays to the ground state by $M1$ transition, with an estimated lifetime of 7 ms.

The CI calculations show that the $4d \rightarrow 4f$ transition in Xe^{5+} $5^2P_{1/2}$ contains two strong lines, while that in

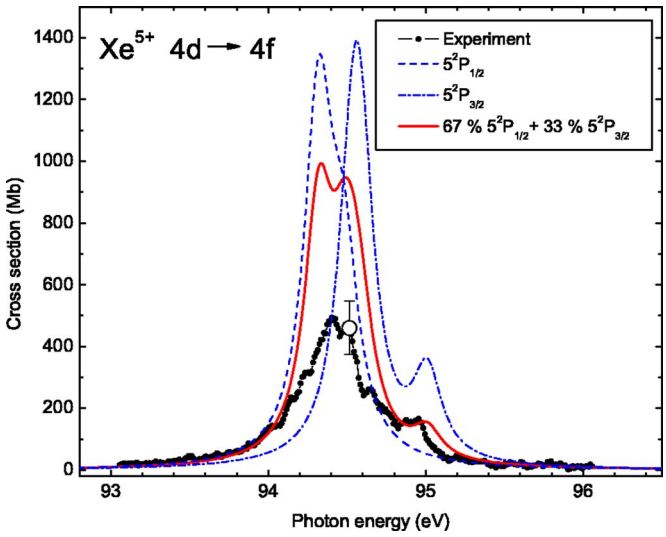

FIG. 2. (Color online) Xe^{5+} photoionization cross sections in the vicinity of the $4d \rightarrow 4f$ transition obtained in experiment (solid curve with black dots) and calculated for the $5^2P_{1/2}$ and $5^2P_{3/2}$ states (dash and dash-dot blue curves, respectively), and for a mixture of 67% ground and 33% metastable ions (solid red curve). See text for details. For the purpose of comparison the theoretical curves have been shifted by −3.32 eV from their original position with respect to the experimental data.

TABLE IV. Transition energies (in eV) and oscillator strengths (in L form) of the strong lines corresponding to the $4d \rightarrow 4f$ and $4d \rightarrow 5f$ transitions in Xe^{5+} $5^2P_{1/2}$ and $5^2P_{3/2}$, from relativistic CI calculations.

	Final state			
Initial state	J	ω	f	Term
$5^2P_{1/2}$	$\frac{3}{2}$	97.64	3.86	$4f\ ^2D_{3/2}$
	$\frac{1}{2}$	97.80	1.88	$4f\ ^2P_{1/2}$
	$\frac{3}{2}$	109.94	0.33	$5f$ —
	$\frac{1}{2}$	110.24	0.80	$5f\ ^2P_{1/2}$
	$\frac{3}{2}$	110.51	1.15	$5f\ ^2D_{3/2}$
$5^2P_{3/2}$	$\frac{3}{2}$	97.85	1.97	$4f\ ^2P_{3/2}$
	$\frac{5}{2}$	97.90	2.93	$4f\ ^2D_{5/2}$
	$\frac{1}{2}$	98.33	0.95	$4f\ ^2S_{1/2}$
	$\frac{3}{2}$	110.54	0.80	$5f\ ^2P_{3/2}$
	$\frac{1}{2}$	110.62	0.40	$5f\ ^2S_{1/2}$
	$\frac{5}{2}$	110.63	1.15	$5f\ ^2D_{5/2}$

Xe^{5+} $5^2P_{3/2}$ contains three strong lines. Their energies and oscillator strengths are given in Table IV. The total oscillator strength of the two lines from the $5^2P_{1/2}$ state is 5.74, while that of the three lines from the $5^2P_{3/2}$ state is 5.84. These numbers are between the HF and RPA values in Table II. The intensities of individual lines in $5^2P_{1/2}$ are in the 2:1 ratio, while those in $5^2P_{3/2}$ relate as 2:3:1. This simple picture follows from the fact that the $4d \rightarrow 4f$ transition produces a hole-particle excitation $4d^{-1}4f$ with the term $^1P_1$ determined by the $E1$ photon. Its total angular momentum is then coupled with the angular momentum j of the "spectator" $5p$ electron, forming either two $\left(j=\frac{1}{2}\right)$ or three $\left(j=\frac{3}{2}\right)$ states. The resulting intensities are proportional to the squares of the corresponding Clebsch-Gordan coefficients.

Similarly, there are two strong $4d \rightarrow 5f$ absorption lines in Xe^{5+} $5^2P_{1/2}$. In this case, however, there is an additional weaker line at lower energy due to configuration mixing. The $4d \rightarrow 5f$ transitions from $5^2P_{3/2}$ contains three strong lines with angular momenta $J=\frac{3}{2}, \frac{1}{2}$, and $\frac{5}{2}$, which appear in a different order to those of the $4d \rightarrow 4f$ lines. The total oscillator strengths of these groups of lines obtained in CI are 2.28 and 2.35. These numbers are again between the HF and RPA values from Table II.

We can now test the effect of the configuration interaction and metastable state on the shape of the line. In Figs. 2 and

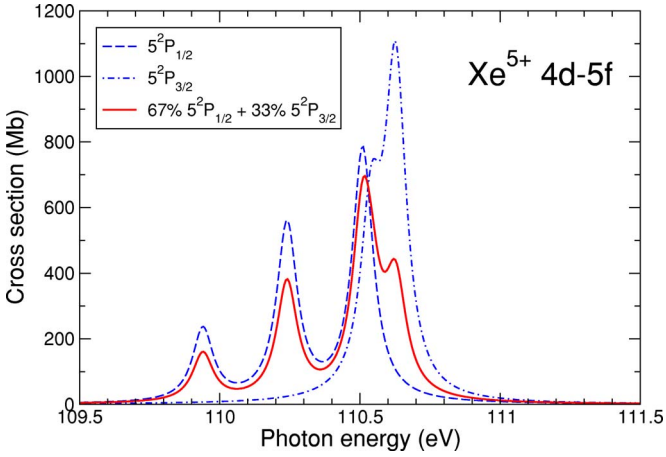

FIG. 3. (Color online) Xe^{5+} photoionization cross sections in the vicinity of the $4d \rightarrow 5f$ transition calculated for the $5^2P_{1/2}$ (blue dashed line) and $5^2P_{3/2}$ (blue dash-dot line) states, and for a mixture of 67% ground and 33% metastable ions (red solid line). See text for details.

3 we show the line shapes obtained by adding the Breit-Wigner contributions of individual transitions from Table IV. The width of the individual lines in the $4d \rightarrow 4f$ and $4d \rightarrow 5f$ groups are assumed to be equal to the RPA values of the corresponding autoionizing widths, 0.220 and 0.0893 eV, respectively. We also use the best RPA oscillator strengths from Table II, and distribute them between the lines proportionally to their CI oscillator strengths. The experimental width of the $4d \rightarrow 4f$ maximum is greater than that of either 5^2P_J state. Hence it is likely that the ion beam contains both species. Figure 2 shows that a mixture of 67% of $5^2P_{1/2}$ and 33% of $5^2P_{3/2}$ states results in a line shape similar to that observed in the experiment. The shape of the $4d \rightarrow 5f$ transition contains three clearly separated peaks. Unlike the $4d \rightarrow 5f$ transition in Xe^{6+}, this structure is mostly due to configuration mixing rather than the effect of metastable species. The latter, though, affects the shape of the main maximum.

C. Photoionization of Xe^{4+}

Figure 4 shows the absolute photoionization cross-section measurements for Xe^{4+} from 89 to 112 eV. The structure centered at around 91 eV has been attributed [20] to resonant excitation of a $4d$ electron into $[4d^9 5s^2 5p^2]\,4f$, $6p$ and $5f$ configurations of Xe^{4+*}, followed by autoionization into the final Xe^{5+} state. The inset in this figure shows the band of interest for EUV lithography, centered at 13.5 nm with a ±2% limit. The peak centered at 102 eV corresponds to $4d \rightarrow 5f$ transitions. The open circles with error bars represent our absolute measurements to which the spectrum was normalized. The cross-section calculations performed by Bizau *et al.* [20] in this energy region agree well for the first resonance; however, for the resonance centered at 102 eV the difference is substantial. Higher resolution measurements for the $4d \rightarrow 4f$ transitions are shown in Fig. 5. These measurements did not further resolve the structure observed in the spectrum, indicating that the resonance structures are broad.

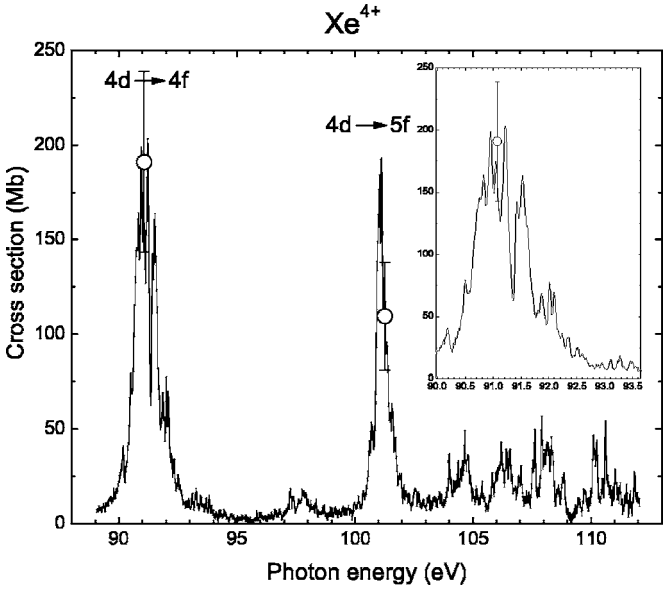

FIG. 4. Our absolute cross-section measurements for photoionization of Xe^{4+} are indicated by open circles with error bars, to which an energy scan performed at a resolution of 60 meV was normalized. The inset shows the 13.5 nm±2% region of interest for EUV lithography on an expanded energy scale.

From the theoretical point of view Xe^{4+} is more problematic. The open $5p^2$ shell makes a RPA calculation less rigorous. It also turns out that in Xe^{4+} the energy of the $4d \rightarrow 6p$ excitation is very close to that of the $4d \rightarrow 4f$ line. This may result in configuration mixing and a more complicated structure of the line, as seen from the experimental results. However, the total oscillator strength is expected to be dominated by the "original" $4d \rightarrow 4f$ strength (in the HF approximation $f^{(L)}_{4d \rightarrow 6p}=0.17$ and $f^{(V)}_{4d \rightarrow 6p}=0.15$). One would thus expect that the total photoabsorption strength in this

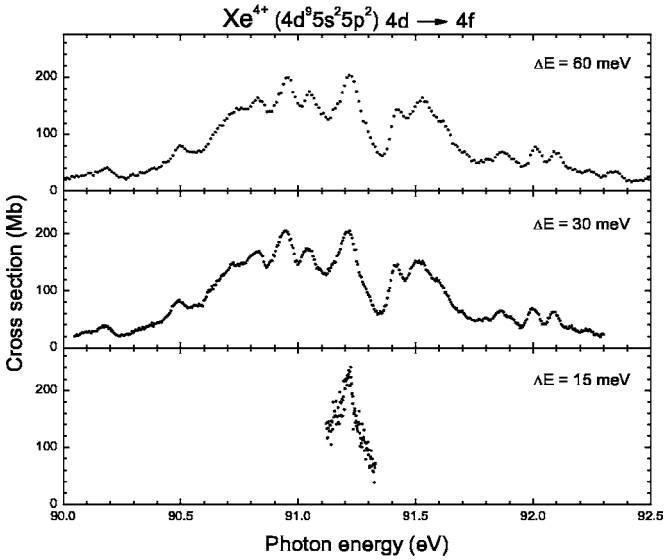

FIG. 5. Comparison plot of the measurements for $4d \rightarrow nf$ transitions in Xe^{4+} at three different energy resolutions (60, 30, and 15 meV).

region is described by the one-channel RPA $4d \rightarrow 4f$ oscillator strength (Table II).

V. DISCUSSION

Autoionizing transitions play an important role on the opacity of optically thick laser-produced plasmas. The spectra presented in Fahy *et al.* [39] and Bruijin *et al.* [13] clearly show this effect, which may impose physical limitations on the brightness of xenon-based light sources working near 13.5 nm. In the LPP xenon emission spectra presented by Fahy *et al.* [39], strong absorption features are seen due to low-charged xenon ions (Xe^{q+} ions for $1 \leqslant q \leqslant 6$). These features, centered at energies of 91.61, 94.40, and 97.43 eV in the Fahy *et al.* spectra correspond to the autoionizing transitions of Xe^{4+}, Xe^{5+}, and Xe^{6+} measured in the present experiment, as clearly indicated in Fig. 6. Other absorption lines observed by Fahy *et al.* were not identified. Our results indicate that they correspond to higher members of the $4d \rightarrow nf$ series for Xe^{4+}, Xe^{5+}, and Xe^{6+}. For example, the $4d \rightarrow 5f$ transition in Xe^{6+} at 115.05 eV (10.778 nm) matches to one of the strongest unassigned absorption features of their emission spectra.

The cross-section scales in Fig. 6 indicate that the intensity of the autoionizing $4d \rightarrow 4f$ transition increases as a function of the charge of the ion. This is a clear example of the collapse of the $4f$ wave function into the core of the ion along the xenon isonuclear sequence. Using the cross sections shown in Fig. 6, the dimensionless oscillator strengths for the $4d \rightarrow 4f$ transitions in Xe^{4+}, Xe^{5+}, and Xe^{6+} have been obtained by calculating the area under the measured peaks using the formula

$$f = 0.9107 \times 10^{-2} \int \sigma(\omega) dE, \tag{3}$$

where $\sigma(\omega)$ is the cross section in Mb and E is the energy in eV. These values are plotted in Fig. 7 (solid circles) along

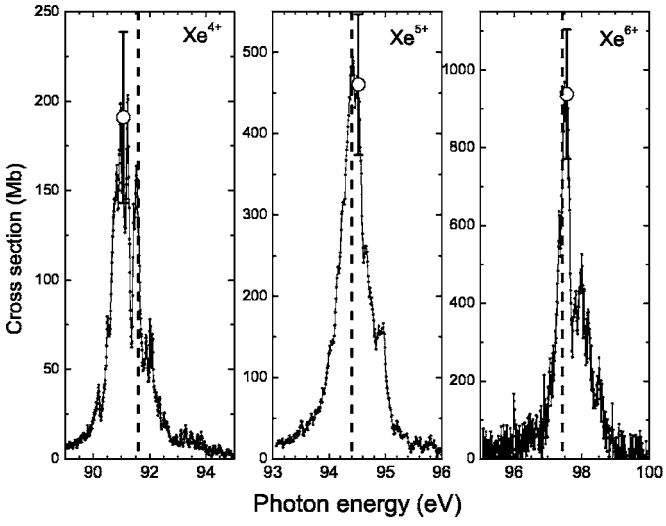

FIG. 6. Absolute photoionization cross-section measurements in the energy ranges of the $4d \rightarrow 4f$ transitions in Xe^{4+}, Xe^{5+}, and Xe^{6+}. The vertical dashed lines indicate the energies at which strong absorption lines have been observed in LPP plasmas [4].

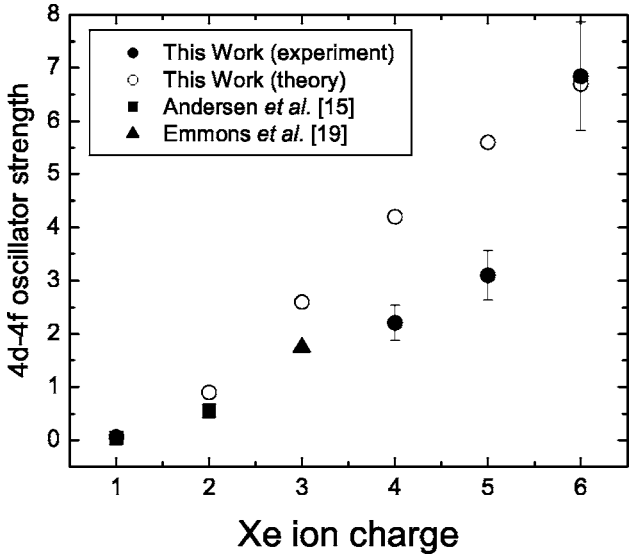

FIG. 7. Comparison of measured $4d \rightarrow 4f$ oscillator strengths from references [15,19] and the present work, with RPA values.

with total oscillator strengths of 0.04 (Xe^{+}) and 0.55 (Xe^{2+}) reported by Andersen *et al.* [15] (solid squares). For the $4d \rightarrow 4f$ transitions in Xe^{3+} an oscillator strength of 1.75 is obtained from the measurements reported by Emmons *et al.*[19] (solid triangle).

The open circles in this plot correspond to the calculated oscillator strengths of the $4d \rightarrow 4f$ transitions. The calculated values show a near-linear dependence on the charge of the ion between Xe^{+} and Xe^{6+}. For Xe^{6+} both $f_{4d \rightarrow 4f}$ and $f_{4d \rightarrow 5f}$ (not shown in the plot) are in good accord with the measurements. On the other hand, the experiment shows a much more rapid drop of the $4d \rightarrow 4f$ oscillator strength as the ion charge decreases. This discrepancy is not easy to explain, given the good agreement between the RPA calculations and experiment for Xe^{6+} and neutral Xe (where it correctly describes the broad resonance in the continuum).

One possibility is that in the ions with an open $5p$ subshell, the $4d \rightarrow 4f$ transition can share its oscillator strength with nearby *satellites*, i.e., other excited states, due to configuration mixing. The ionization cross sections of Xe^{+} and Xe^{2+} [15] give some support for such an interpretation. While they do show sharp peaks of the $4d \rightarrow nf$ lines, these peaks by no means account for the total oscillator strength *below* the $4d$ ionization threshold. A very large portion of this strength takes the form of a background, possibly containing numerous smaller resonances. Given that all other *direct* dipole transitions apart from $4d \rightarrow nf$ and $4d \rightarrow np$ are weak in this photon energy range, one may infer that the oscillator strengths of these transitions are redistributed between a large number of satellite lines. However, the present measurements for Xe^{5+} and Xe^{4+} did not reveal any strong additional lines in the neighborhood of the $4d \rightarrow 4f$ resonances. Hence the discrepancy between experiment and theory for intermediate charge states remains an open question.

VI. SUMMARY AND CONCLUSIONS

Absolute photoionization cross-section measurements for some of the $4d \rightarrow nf$ transitions in Xe^{4+}, Xe^{5+}, and Xe^{6+} have been measured at a resolution of 60 meV. Higher-resolution measurements were also performed, but they do not indicate additional structure. Comparison with RPA and CI calculations indicate that the ion source is also emitting metastable states which have to be accounted for in the theory in order to adequately interpret the measurements.

The discrepancy between the experimental and theoretical oscillator strengths of the strong $4d \rightarrow 4f$ transition for Xe^{q+} with $q=3$, 4, and 5, remains a puzzle. One might suspect that RPA is less accurate for open-shell systems. However, the main correlation effect in the $4d$ photoabsorption is the interaction of the ten $4d$ electrons, which should be described well by the RPA.

The positions of the photoionization resonances for the xenon ions match those of the absorption lines observed in LPP. These absolute values extend the utility of benchmark atomic calculations in the sophisticated codes being developed for the modeling of EUV lithography light sources.

ACKNOWLEDGMENTS

The authors are indebted to Bruce Rude of the Advanced Light Source for technical support provided during the experiment. This research was supported in part by a grant from International SEMATECH to the NIST-EBIT group, and in part by the Division of Chemical Sciences, Geosciences and Biosciences of the U.S. Department of Energy under Contract No. DE-FG02-03ER15424. MK acknowledges support of the International Research Centre for Experimental Physics (Queen's University).

[1] V. Bakashi, ''EUV Sources for Lithography (PM149)'', SPIE, Bellingham, WA, Feb. 2006.
[2] N. Bwering, M. Martins, W. N. Partlo, and I. V. Fomenkov, J. Appl. Phys. **95**, 16 (2004).
[3] L. Juschkin, A. Chuvatin, S. V. Zakharov, S. Ellwi, and H-J. Kunze, J. Phys. D **35**, 219 (2002).
[4] G. O'Sullivan, J. Phys. B **15**, L765 (1982).
[5] J. Blackburn, P. K. Carroll, J. Costello, and G. O'Sullivan, J. Opt. Soc. Am. **73**, 1325 (1983).
[6] V. Banine and R. Moors, Proc. SPIE **4343**, 203 (2001).
[7] R. Lebert, K. Bergmann, L. Juschkin, O. Rosier, and W. Neff, Proc. SPIE **4343**, 215 (2001).
[8] A. Hassanein, V. Sizyuk, V. Tolkach, V. Morozov, T. Sizyuk, and B. Rice, Proc. SPIE **5374**, 413 (2004).
[9] A. Hassanein, V. Sizyuk, V. Tolkach, V. Morozov, and B. Rice, J. Microlithogr., Microfabr., Microsyst. **3**, 130 (2004).
[10] F. Gilleron, M. Poirier, T. Blenski, M. Shmidt, and T. Ceccotti, J. Appl. Phys. **94**, 2086 (2003).
[11] Thomas Kruecken (private communication).
[12] M. Kanouff, H. Shields, L. Bernandez, D. Chenoweth, and G. Kubiak, J. Appl. Phys. **90**, 3726 (2001).
[13] R. de Bruijn, K. Koshelev, G. Kooijman, E. Simona Toma, and F. Bijkerk, J. Quant. Spectrosc. Radiat. Transf. **81**, 97-105 (2003).
[14] Ahmed Hassanein (private communication).
[15] P. Andersen, T. Andersen, F. Folkmann, V. K. Ivanov, H. Kjeldsen, and J. B. West, J. Phys. B **34**, 2009 (2001).
[16] Y. Itoh, A. Ito, M. Kitajima, T. Koizumi, T. M. Kojima, H. Sakai, M. Sano, and N. Watanabe, J. Phys. B **34**, 3493 (2001).
[17] T. Koizumi, Y. Awaya, A. Fujino, Y. Itoh, M. Kitajima, T. M. Kojima, M. Oura, R. Okuma, M. Sano, T. Seikioka, N. Watanabe, and F. Koike, Phys. Scr. **T73**, 131 (1997).
[18] E. D. Emmons, Masters thesis, University of Nevada, Reno, 2004 (unpublished).
[19] E. D. Emmons, A. Aguilar, M. F. Gharaibeh, S. W. J. Scully, R. A. Phaneuf, A. L. D. Kilcoyne, A. S. Schlachter, I. Álvarez, C. Cisneros, and G. Hinojosa, Phys. Rev. A **71**, 042704 (2005).
[20] J. M. Bizau, J.-M. Esteva, D. Cubaynes, F. J. Wuilleumier, C. Blancard, A. C. Fontaine, C. Couillaud, J. Lachkar, R. Marmoret, C. Remond, and M. Delaunay, Phys. Rev. Lett. **84**, 435 (2000).
[21] B. Peart, J. G. Stevenson, and K. Dolder, J. Phys. B **6**, 146 (1973).
[22] I. C. Lyon, B. Peart, J. B. West, and K. Dolder, J. Phys. B **19**, 4137 (1986).
[23] T. Koizumi, Y. Itoh, M. Sano, M. Kimura, T. M. Kojima, S. Kravis, A. Matsumoto, M. Oura, T. Sekioka, and Y. Awaya, J. Phys. B **28**, 609 (1995).
[24] H. Kjeldsen, F. Folkmann, H. Knudsen, M. S. Rasmussen, J. B. West, and T. Andersen, J. Phys. B **32**, 4457 (1999).
[25] A. M. Covington, A. Aguilar, I. R. Covington, M. F. Gharaibeh, G. Hinojosa, C. A. Shirley, R. A. Phaneuf, I. Alvarez, C. Cisneros, I. Dominguez-Lopez, M. M. SantAnna, A. S. Schlachter, B. M. McLaughlin, and A. Dalgarno, Phys. Rev. A **66**, 062710 (2002).
[26] J. B. West, J. Phys. B **34**, R45 (2001).
[27] H. Kjeldsen, P. Andersen, F. Folkmann, J. Hansen, M. Kitajima, and T. Andersen, J. Phys. B **35**, 2845 (2002).
[28] A. Cummings, C. McGuinness, G. O'Sullivan, J. T. Costello, J. P. Mosnier, and E. T. Kennedy, Phys. Rev. A **63**, 022702 (2001).
[29] G. C. King, M. Tronc, F. H. Read, and C. Bradford, J. Phys. B **10**, 2479 (1977).
[30] M. Domke, K. Schulz, G. Remmers, G. Kaindl, and D. Wintgen, Phys. Rev. A **53**, 1424 (1996).
[31] M. Ya. Amusia and N. A. Cherepkov, Case Stud. At. Phys. **5**, 47 (1975).
[32] M. Ya. Amusia, *Atomic Photoeffect* (Plenum Press, New York, 1990).
[33] M. Ya. Amusia, N. A. Cherepkov, L. V. Chernysheva, and S. T. Manson, J. Phys. B **33**, L37 (2000).
[34] M. Y. Amusia, L. V. Chernysheva, G. F. Gribakin, and K. L. Tsemekhman, J. Phys. B **23**, 393 (1990).

[35] A. A. Radzig and B. M. Smirnov, *Reference Data on Atoms, Molecules, and Ions, Springer Series in Chemical Physics*, Vol. 31 (Springer, Berlin, 1985).
[36] V. F. Bratsev, G. B. Deyneka, and I. I. Tupitsyn, Bull. Acad. Sci. USSR, Phys. Ser. (Engl. Transl.) **41**, 173 (1977).
[37] S. A. Kotochigova and I. I. Tupitsyn, J. Phys. B **20**, 4759 (1987).
[38] In principle, the CI method can be combined with the many-body theory to achieve a better description of the correlations effects, see, e.g., S. G. Porsev, Yu. G. Rakhlina, and M. G. Kozlov, J. Phys. B **32**, 1113 (1999); Phys. Rev. A **60**, 2781 (1999).
[39] K. Fahy, P. Dunne, L. McKinney, G. O'Sullivan, E. Sokell, J. White, A. Aguilar, J. M. Pomeroy, J. N. Tan, B. Blagojević, E-O LeBigot, and J. D. Gillaspy, J. Phys. D **37**, 3225 (2004).